



Widely tunable narrow-linewidth lasers with booster amplification on silicon photonics

YANG LIU,^{1,*}  YE CHEN,¹  LAURENS BOGAERT,¹  EMADREZA SOLTANIAN,¹  EVANGELIA DELLI,¹ GUY LEPAGE,² PETER VERHEYEN,² JORIS VAN CAMPENHOUT,² GEERT MORTHIER,¹  GUNTHER ROELKENS,¹ AND JING ZHANG¹ 

¹Photonics Research Group, INTEC, Ghent University - imec, 9052 Ghent, Belgium

²IMEC, Kapeldreef 75, 3001 Heverlee, Belgium

*yangliu.liu@ugent.be

Abstract: Achieving high-power, narrow-linewidth, and low-intensity-noise (RIN) widely tunable lasers on silicon photonics (SiPh) platforms remains a critical challenge for transformative photonic applications. In this work, we present the micro-transfer printing of double-ridge InP/InGaAs semiconductor optical amplifiers (SOAs) onto a silicon photonics platform to realize on-chip widely tunable lasers. The double-ridge SOA structure enables simultaneous control of laser cavity gain and laser output optical amplification. The resulting tunable laser exhibits a wide tuning range exceeding 51 nm and delivers a waveguide-coupled output power of 10 mW per wavelength. Additionally, the device achieves a narrow linewidth of 1.6 kHz and a low RIN of approximately -140 dB/Hz. These characteristics underscore the suitability of the device for demanding applications in wavelength-division multiplexing systems and photonic sensing. This approach demonstrates a viable pathway toward compact and high-performance laser-based photonic systems-on-chip.

© 2025 Optica Publishing Group under the terms of the [Optica Open Access Publishing Agreement](#)

1. Introduction

Silicon photonics has emerged as a transformative platform for photonic integrated circuits (PICs), benefiting from CMOS-compatible manufacturing to deliver compact, cost-effective, and scalable solutions [1–5]. By leveraging heterogeneous integration techniques such as micro-transfer printing and wafer bonding, the integration of non-CMOS-compatible functional devices, including III-V light sources, in-line optical amplifiers, electro-optic modulators, optical isolators, and more is enabled [6–11]. This capability facilitates the development of fully integrated photonic systems on a silicon platform, unlocking a wide range of complex and advanced functionalities, and paving the way for innovative applications. Among these, widely tunable lasers are crucial for next-generation tele/data communication systems, as well as in photonic sensing applications [12–17].

Especially, tunable lasers with narrow linewidth and low relative intensity noise (RIN) are indispensable. Narrow linewidth is critical for coherent optical communication, as it supports high-order modulation formats (e.g. 64-QAM), enabling ultra-high-speed data transmission with superior spectral efficiency [18–21]. Simultaneously, low RIN ensures high quality signal transmission in direct detection systems [22–24]. Moreover, in wavelength-division multiplexing (WDM) systems, achieving high and uniform output power across all wavelengths is vital to minimize inter-channel power imbalances [25–27]. Power variations can amplify nonlinear effects, such as cross-phase modulation (XPM) and four-wave mixing (FWM), ultimately degrading transmission quality and limiting system performance [28–30].

To address these challenges, we demonstrate the integration of double-ridge InP/InGaAs multi-quantum well SOA coupons on a silicon photonic integrated circuit to form high-performance

widely tunable lasers. As the active gain element, the innovative double-ridge SOA structure uniquely combines two ridges with distinct functionalities: one operates within the laser cavity to provide gain, while the other on the output path functions as a booster amplifier. For the passive elements, the tunable laser incorporates a high-quality, well-designed silicon laser cavity on the SiPh platform featuring a thermally tunable Vernier filter and a broadband Sagnac loop mirror, achieving wide wavelength tuning and narrow-linewidth operation.

Through the synergistic combination of the dual-function amplifiers in the active region and the precise mode control in the passive cavity region, we achieve high-performance, widely tunable lasers with narrow linewidth, low RIN, and uniform power output on the SiPh platform. This approach enhances integration density and optimizes the utilization of costly III-V materials, providing a more efficient and scalable laser design for silicon photonics platforms.

2. Design and fabrication

To realize the widely tunable lasers on SiPh, micro-transfer printing was employed to decouple the III-V fabrication process from the silicon photonics (SiPh) platform. The dual-ridge InP/InGaAs SOAs are pre-fabricated on their original epitaxial wafers, which were grown using metal-organic chemical vapor deposition (MOCVD) and comprise an active layer stack with an n-InP contact layer, InAlGaAs quantum wells, barriers, separate confinement heterostructure (SCH) layers, a p-InP cladding layer, and a p-InGaAs contact layer [31]. In contrast to conventional single-ridge III-V active devices typically used for heterogeneous integration [32–35], the InP/InGaAs semiconductor optical amplifier coupons in the tunable lasers feature a dual-ridge architecture, as shown in Fig. 1(a). It comprises a shared n-InP contact layer with two InP/InAlGaAs active ridges defined on top. Each ridge is 3 μm wide and both are separated by 20 μm . The structure was defined in our lab through standard III-V fabrication processes, such as lithography and inductively coupled plasma (ICP) etching. P-metal contacts for the two ridges and the n-metal contact were deposited using electron beam evaporation.

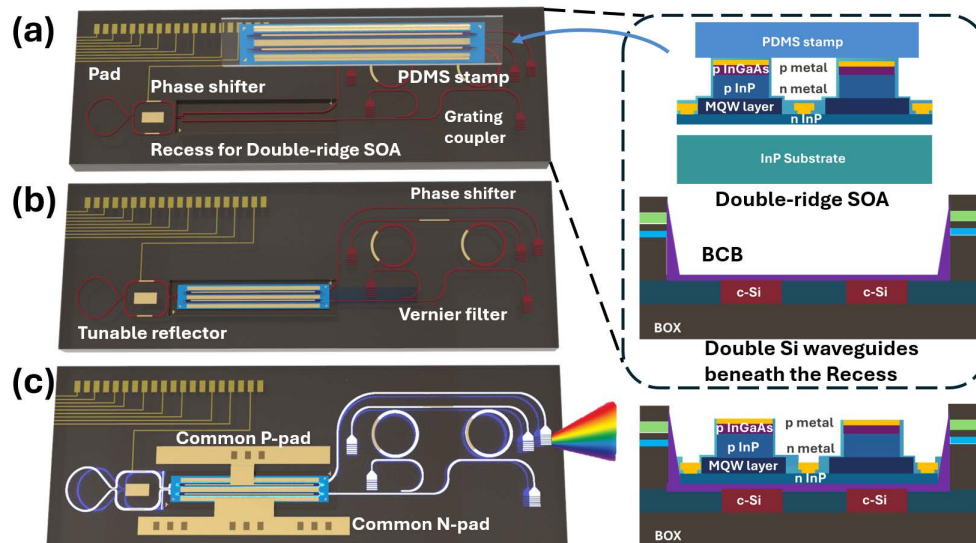


Fig. 1. The schematic process flow for the integration of InP multi-quantum well active devices on a SiPh platform, and the cross-section of the dedicated recess before and after printing the double-ridge SOA.

The silicon waveguide circuits were fabricated on SOI wafers with 400nm thick Si device layer using imec's SiPh pilot-line. This platform includes a 400 nm crystalline silicon (c-Si) device layer on a 2 μm buried oxide (BOX) layer. The backend-of-line (BEOL) stack features metal interconnect layers, heaters and exposed aluminum bond pads. To integrate the III-V devices, recesses were etched into the SiPh backend, as shown in Fig. 1(a). A thin adhesive layer of benzocyclobutene (BCB), around 40-100 nm thick, was applied to facilitate high-yield transfer printing.

On the passive silicon photonics circuit, the Vernier filter is implemented using two thermally tunable micro-ring resonators (MRRs) with slightly different radii (25 μm and 27 μm). The Vernier configuration expands the effective free spectral range (FSR) to 51 nm, enabling a broader tuning range compared to the individual resonators. Additionally, a thermally tunable phase shifter placed between the two MRRs adjusts the optical path length, ensuring precise resonance alignment and enhancing the frequency selectivity of the filter. To manage cavity reflectivity and optimize output coupling, a tunable Sagnac loop mirror is employed. By controlling the phase difference between the arms of the Mach-Zehnder interferometer (MZI) within the loop, the reflectivity is dynamically tuned. This adjustment allows for precise optimization of the mirror loss, reducing the threshold current and improving the slope efficiency.

Using a wafer-scale micro-transfer printing tool (Amicra Nano), eight double-ridge devices were simultaneously picked by a polydimethylsiloxane (PDMS) stamp patterned with a periodic array post structure and precisely placed into the pre-etched recesses on the silicon substrate, ensuring efficient optical coupling, as shown in Fig. 1(b). After placement, standard metallization processes were carried out to create common p- and n-side electrode pads, effectively connecting the double-ridge SOAs to the on-chip metal tracks of the SiPh platform, as shown in Fig. 1(c).

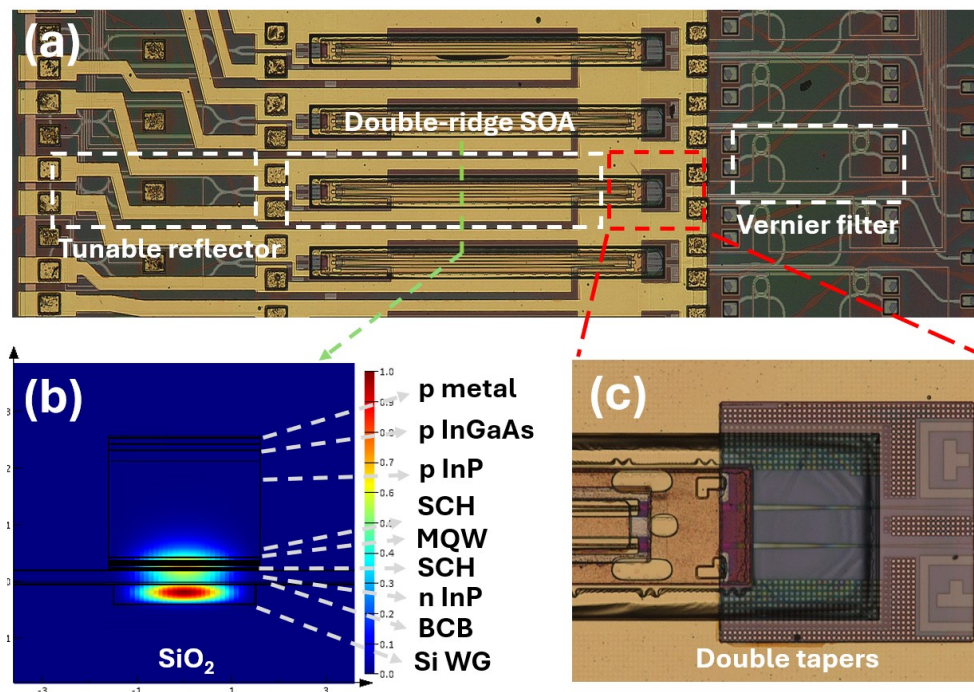


Fig. 2. (a) The microscope image of the double-ridge devices integrated into the SiPh wafer recesses, (b) hybrid optical mode profile in the middle of a single ridge, (c) close-up view of the double-taper regions.

Figure 2(a) shows a microscope image of the double-ridge devices integrated into the SiPh wafer recesses, along with a close-up view of the double-taper regions (Fig. 2(c)).

Once integrated, one ridge is aligned with the silicon waveguide between the thermally tunable Vernier filter and the Sagnac loop mirror. This ridge serves as the gain medium for the on-chip widely tunable laser, providing optical gain for the resonant modes selected by the passive silicon cavity. As shown in Fig. 2(b), the hybrid optical mode profile at the center of each single ridge indicates an optical confinement of approximately 12.6% in the MQW region (quantum wells + barriers), as simulated using the Ansys Lumerical FDE solver. This design is intended to achieve a balance between gain and saturation power. The output waveguide after the Sagnac loop mirror is guided beneath the second ridge, where the light is coupled into the active layer of the second ridge via a high-tolerance vertical taper structure for amplification. The amplified light is coupled back into the waveguide, efficiently boosting the output signal.

3. Characterization and discussion

To thoroughly investigate the characteristics of the double-ridge InP-on-Si tunable lasers, a series of measurements were carried out. The lasers were placed on a temperature-controlled stage for all measurements. The devices under test were optically probed using cleaved standard single mode fibers and electrically contacted using DC probe needles. Keithley 2400 SourceMeters were used to drive the active III-V devices and all the micro-heaters. The output of the laser was characterized using an Optical Spectrum Analyzer (OSA, Agilent 86140B) set to a resolution bandwidth (RBW) of 0.1 nm.

As shown in Fig. 3(a), the double-ridge SOA structure exhibits a differential resistance of 8-9 Ω . Since the two active ridges are connected in parallel, the drive current is divided between the cavity gain ridge and the booster ridge. Figure 3(b) illustrates that the threshold current for lasing in the gain ridge varies from 66 mA to 72 mA (half of the value indicated in the graph), depending on the resonant wavelength. This small variation in threshold current across different longitudinal modes arises from the wavelength-dependent gain spectrum of the active multiple quantum well (MQW) medium. As the resonant wavelength is tuned by the Vernier filter from 1540.8 nm to 1556.7 nm, aligning closer to the peak of the MQW gain spectrum, the waveguide-coupled output power increases from 6.9 mW to 10.1 mW. This improvement is attributed to the combined effects of laser gain and booster amplification within the single double-ridge coupon, where the gain ridge and amplification ridge work in synergy to enhance the overall output power. The kinks in the LI-curve are attributed to self-heating in the laser cavity, thereby changing the alignment of the longitudinal modes with the Vernier filter transmission spectrum.

By tuning the Vernier filter, we can traverse the entire spectral range of the tunable laser, as shown in Fig. 4(a). The tuning range spans from 1526.1 nm to 1577.1 nm, achieving a total tuning range exceeding 51 nm. Each spectral line exhibits a side-mode suppression ratio (SMSR) of approximately 40 dB, indicating excellent single-mode operation. Regarding linewidth performance, Fig. 4(b) presents the linewidth for each spectral line, while Fig. 4(c) shows the frequency noise spectrum and instantaneous linewidth (Ins LW) at the center wavelength of the tunable laser, measured using the OE4000 laser phase noise analyzer. The results indicate that the linewidth can be as narrow as 1671 Hz, with 9 out of the 14 measured wavelengths demonstrating linewidths below 3.5 kHz. This significant linewidth reduction is attributed to the Vernier filter's effective optical length near resonance [37,38]. The effective cavity length L_{eff} is defined by the following relation [39]:

$$L_{\text{eff}} = \left(\frac{L_o}{L_{\text{ring}}} + \frac{1 - \kappa^2}{\kappa^2} \right) L_{\text{ring}} \quad (1)$$

where L_{ring} is the length of the resonator cavity, L_o is the length of the external loop, and κ represents the out-coupling ratio. The introduction of the micro-ring resonator significantly

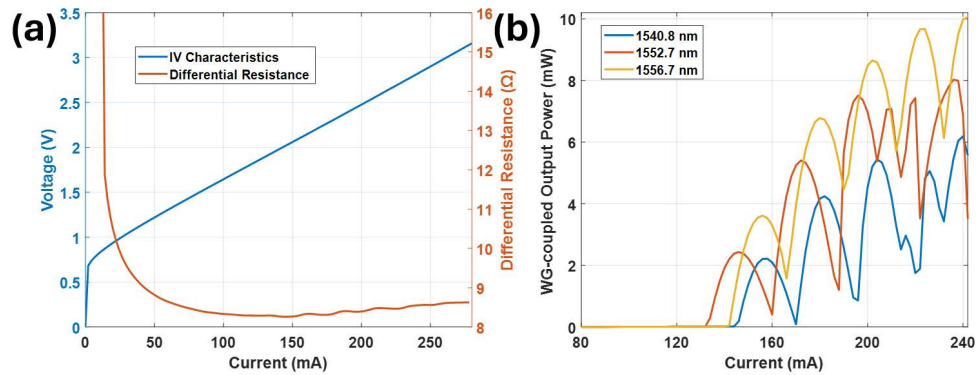


Fig. 3. (a) Current-voltage (IV) characteristics and differential resistance of the double-ridge tunable laser, (b) WG-coupled output power as a function of current for the tunable laser at 1540.8 nm, 1552.7 nm, and 1556.7 nm.

extends the effective cavity length, with resonance-induced enhancement playing a vital role in achieving the observed high spectral purity and narrow linewidths [40–42]. Specifically, the effective cavity lengths of micro-rings with radii of 25 μm and 27 μm are extended to 2.4 mm and 2.6 mm, respectively.

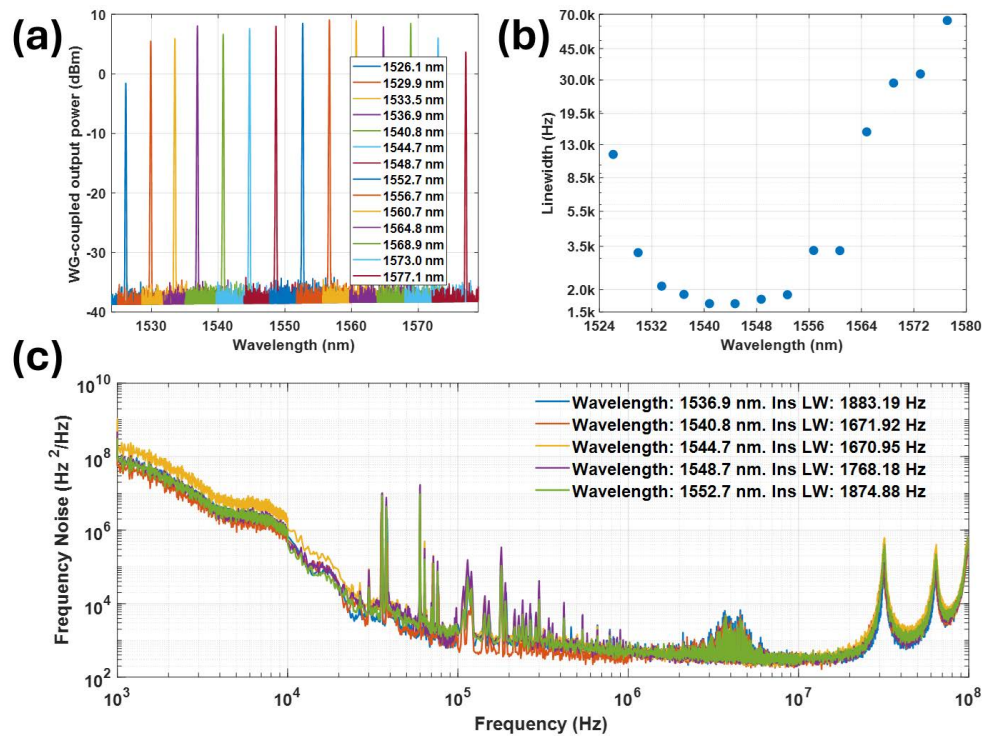


Fig. 4. (a) Optical spectrum of the tunable lasers at 20 °C. (b) Linewidth of each wavelength of the tunable lasers. (c) Frequency noise spectrum of the central wavelengths.

In laser operation, the recombination and generation of carriers and photons inherently lead to instantaneous fluctuations in photon density. These fluctuations cause variations in the output

power, referred to as relative intensity noise (RIN). High RIN levels can adversely affect optical communication systems increasing the bit error rate (BER). To measure the RIN of each spectral line of the tunable lasers, a dedicated setup was constructed, as illustrated in Fig. 5(a). The optical signal from the laser was first converted into an electrical signal using a high-speed photodetector (PD) with co-integrated transimpedance amplifier (TIA) (Discovery DSCR409). The resulting electrical signal was passed through a DC block to remove the DC component. The RF signal was then amplified using an RF amplifier (SHF S804 B) before being analyzed by an Electrical Spectrum Analyzer (ESA, Keysight N9010A) to evaluate the laser's RIN. It is important to note that the measured noise includes contributions from various sources, including the laser's intrinsic RIN, the photodetector's shot noise, and the thermal noise from the RF amplifier and TIA.

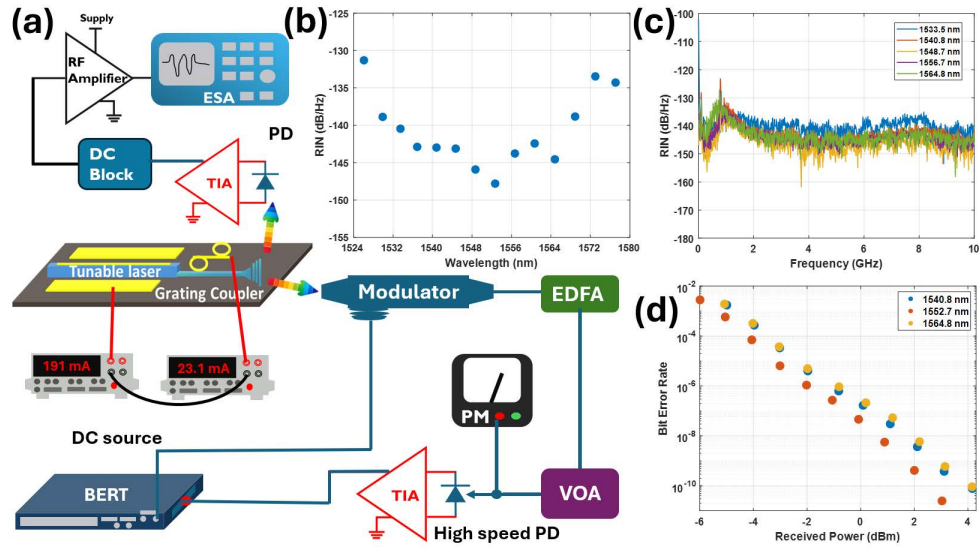


Fig. 5. (a) Schematic diagram of the experimental setup used for RIN noise testing and high-speed transmission testing, (b) Average RIN values between 2 GHz and 3 GHz, (c) Measured RIN spectra of the wavelengths spaced 8 nm apart within the tunable laser spectrum, (d) Bit Error Rate as a function of received optical power for the tunable laser at 1540.8 nm, 1552.7 nm, and 1556.7 nm.

After calibrating the system noise contributions, the intrinsic RIN of the laser was determined. Figure 5(b) shows the average RIN values from 2 GHz to 3 GHz for each wavelength of the tunable lasers. Among them, 9 out of the 14 wavelengths exhibit RIN values below -140 dB/Hz. Figure 5(c) presents the RIN spectra for wavelengths spaced 8 nm apart within the tunable laser spectrum. A prominent RIN peak around 1 GHz is observed, corresponding to the relaxation oscillation frequency of the tunable laser. The relaxation oscillation frequency (f_r) is fundamentally governed by the coupled dynamics of the photon density ($S(t)$) and the carrier density ($N(t)$), which are strongly influenced by the cavity structure. Using the small-signal equations for $S(t)$ and $N(t)$ [43–45], the relationship between the relaxation oscillation frequency and the cavity structure can be expressed as:

$$(2\pi f_r)^2 = \frac{S_0 G_{th} \frac{dG}{dN}}{1 + \frac{L_{eff}}{L_{gain}}} \quad (2)$$

where S_0 represents the steady-state photon density, L_{eff} and L_{gain} are the lengths of the effective and active regions of the cavity, respectively, and G_{th} is the threshold gain. The term $1 + \frac{L_{\text{eff}}}{L_{\text{gain}}}$ highlights the critical role of the passive cavity length (L_{passive}) in reducing the effective coupling between the photon and carrier densities. A longer passive cavity introduces additional delay in the feedback loop, thereby significantly lowering the relaxation oscillation frequency. In our system, this effect reduces f_r to approximately 1 GHz, consistent with the extended photon lifetime in a cavity featuring a substantial passive section.

Since the RIN noise varies slightly across different wavelengths, the performance of each wavelength will differ slightly when the laser is used to support high-speed transmission systems. To evaluate this, we directed the output of the tunable laser at different wavelengths into a high-speed transmission system operating at a baud rate of 12 Gbaud with a PRBS15 signal, as shown in Fig. 5(a). The Anritsu BERTWave MP2101A was employed to generate the pattern pulse (PPG) for driving the modulator and to perform BER testing. Meanwhile, the optical power of each wavelength entering the modulator was maintained at -4.3 dBm to ensure consistent conditions for evaluating the performance differences among the wavelengths.

The results presented in Fig. 5(d), indicate that when providing enough received power into the PD, the BER falls below the measurable lower limit of the BER tester. This demonstrates that the tunable lasers can support a bit-error-free transmission system. And at the same received power, the BER for the 1552.7 nm wavelength is consistently lower than for the 1540.8 nm and 1564.8 nm wavelengths. This difference can be attributed to the lower RIN noise observed for 1552.7 nm, as shown in Fig. 5(b). Being at the center of the gain spectrum of the MQW active layers in the double-ridge laser, a reduced RIN noise is obtained. In contrast, the BER values for 1540.8 nm and 1564.8 nm are similar (but higher) at the same received power, as their RIN noise levels are comparable. Consequently, these wavelengths exhibit similar performance in supporting high-speed transmission systems. To contextualize the performance of our double-ridge tunable laser, Table 1 presents a comparison of key metrics against representative state-of-the-art III-V/Si tunable lasers, including designs with and without integrated SOA boosters. Our device demonstrates a competitive tuning range, high waveguide-coupled output power, and notably low linewidth and RIN, highlighting the benefits of the proposed architecture and micro-transfer printing approach.

Table 1. Comparison of Key Performance Metrics for Tunable InP/Si Lasers based on Heterogeneous Integration

Device Type	Tuning Range	Output Power	Linewidth	RIN	SMSR
Single ridge tunable laser [12]	40 nm	1 mW (WG-coupled)	550 kHz	-	40 dB
Single ridge + SOA booster [36]	50 nm	10 mW (Fiber-coupled)	259 kHz	-	50 dB
Double ridge tunable laser (this work)	51 nm	10 mW (WG-coupled)	1.6 kHz	-140 dB/Hz	40 dB

The double-ridge tunable laser exhibits an electrical power consumption of approximately 684 mW under optimal output conditions (with a drive current of 120 mA per ridge), corresponding to a wall-plug efficiency of 1.46%. In addition, wavelength tuning is achieved by varying the current applied to one of the ring heaters in the vernier filter from 0 mA to 32 mA, leading to an additional tuning power consumption ranging from 0 to 46 mW. To improve overall energy efficiency, we plan in future iterations to electrically separate the p-electrodes of the two ridges. This will allow independent control of the gain section and the booster, enabling optimized biasing conditions for each and reducing unnecessary power dissipation. We will also explore further optimization of the device structure, including incorporating thermal vias into the substrate to lower the overall thermal impedance, thereby reducing self-heating and enhancing the high-temperature performance of the devices, as well as further reduce the series resistance of the III-V device.

4. Conclusion

In this work, we have demonstrated the micro-transfer printing of InP/InGaAs double-ridge active devices onto a silicon photonics platform, achieving high-performance tunable lasers characterized by a waveguide-coupled output power of 10 mW, a minimum linewidth of 1.6 kHz, a broad tuning range exceeding 51 nm, and low relative intensity noise of approximately -140 dB/Hz, enabling high-speed, bit-error-free WDM transmission systems. The unique double-ridge SOA architecture provides a versatile solution for enhancing integration density without compromising device performance. Our results pave the way for the next generation of integrated photonic circuits on silicon platforms, offering a practical route toward high-performance and densely integrated photonic systems.

Funding. European Union grant CALADAN (825453); the EU project grant MedPhab (871345); Dutch National Growth Fund PhotonDelta Project.

Disclosures. The authors declare that there are no conflicts of interest related to this article.

Data availability. Data underlying the results presented in this paper are not publicly available at this time but may be obtained from the authors upon reasonable request.

References

1. S. Shekhar, W. Bogaerts, L. Chrostowski, *et al.*, “Roadmapping the next generation of silicon photonics,” *Nat. Commun.* **15**(1), 751 (2024).
2. M. Moralis-Pegios, G. Giamougiannis, A. Tsakyridis, *et al.*, “Perfect linear optics using silicon photonics,” *Nat. Commun.* **15**(1), 5468 (2024).
3. D. J. Blumenthal, R. Heideman, D. Geuzebroek, *et al.*, “Silicon nitride in silicon photonics,” *Proc. IEEE* **106**(12), 2209–2231 (2018).
4. W. Bogaerts and L. Chrostowski, “Silicon photonics circuit design: methods, tools and challenges,” *Laser Photonics Rev.* **12**(4), 1700237 (2018).
5. D. Thomson, A. Zilkie, J. E. Bowers, *et al.*, “Roadmap on silicon photonics,” *J. Opt.* **18**(7), 073003 (2016).
6. L. Yang, Z. Jing, B. Laurens, *et al.*, “Micro-transfer printing of o-band inas/gaas quantum-dot soas on silicon photonic integrated circuits,” *Photonics Res.* **13**(5), 1341–1352 (2025).
7. G. Roelkens, J. Zhang, L. Bogaert, *et al.*, “Present and future of micro-transfer printing for heterogeneous photonic integrated circuits,” *APL Photonics* **9**(1), 010901 (2024).
8. G. Roelkens, J. Zhang, L. Bogaert, *et al.*, “Micro-transfer printing for heterogeneous si photonic integrated circuits,” *IEEE J. Sel. Top. Quantum Electron.* **29**(3: Photon. Elec. Co-Inte. and Ad), 1–14 (2023).
9. R. Loi, J. O’Callaghan, B. Roycroft, *et al.*, “Micro-transfer-printing of inp photonic devices to silicon photonics,” in *2019 Photonics & Electromagnetics Research Symposium-Spring (PIERS-Spring)*, (IEEE, 2019), pp. 242–248.
10. X. Luo, Y. Cheng, J. Song, *et al.*, “Wafer-scale dies-transfer bonding technology for hybrid iii-v-on-silicon photonic integrated circuit application,” *IEEE J. Sel. Top. Quantum Electron.* **22**(6), 443–454 (2016).
11. Y. Liu, Z. Li, F. B. Atar, *et al.*, “Integration of high-performance ingaas/gan photodetectors by direct bonding via micro-transfer printing,” *ACS Appl. Mater. Interfaces* **16**(8), 10996–11002 (2024).
12. J. Zhang, Y. Li, S. Dhoore, *et al.*, “Unidirectional, widely-tunable and narrow-linewidth heterogeneously integrated iii-v-on-silicon laser,” *Opt. Express* **25**(6), 7092–7100 (2017).
13. Y. Wan, S. Zhang, J. C. Norman, *et al.*, “Tunable quantum dot lasers grown directly on silicon,” *Optica* **6**(11), 1394–1400 (2019).
14. T. Ferrotti, B. Blampey, C. Jany, *et al.*, “Co-integrated 1.3 μm hybrid iii-v/silicon tunable laser and silicon mach-zehnder modulator operating at 25gb/s,” *Opt. Express* **24**(26), 30379–30401 (2016).
15. M. A. Butt, N. L. Kazanskiy, S. N. Khonina, *et al.*, “A review on photonic sensing technologies: status and outlook,” *Biosensors* **13**(5), 568 (2023).
16. S. Pirandola, B. R. Bardhan, T. Gehring, *et al.*, “Advances in photonic quantum sensing,” *Nat. Photonics* **12**(12), 724–733 (2018).
17. V. M. Passaro, C. De Tullio, B. Troia, *et al.*, “Recent advances in integrated photonic sensors,” *Sensors* **12**(11), 15558–15598 (2012).
18. A. Malik, C. Xiang, L. Chang, *et al.*, “Low noise, tunable silicon photonic lasers,” *Appl. Phys. Rev.* **8**(3), 031306 (2021).
19. P. A. Morton, C. Xiang, J. B. Khurgin, *et al.*, “Integrated coherent tunable laser (ictl) with ultra-wideband wavelength tuning and sub-100 hz lorentzian linewidth,” *J. Lightwave Technol.* **40**(6), 1802–1809 (2022).
20. M. Seimetz, “Laser linewidth limitations for optical systems with high-order modulation employing feed forward digital carrier phase estimation,” in *optical fiber communication conference*, (Optica Publishing Group, 2008), p. OTuM2.
21. C. Xiang, W. Jin, O. Terra, *et al.*, “3d integration enables ultralow-noise isolator-free lasers in silicon photonics,” *Nature* **620**(7972), 78–85 (2023).

22. M. Faugeron, M. Tran, O. Parillaud, *et al.*, “High-power tunable dilute mode dfb laser with low rin and narrow linewidth,” *IEEE Photonics Technol. Lett.* **25**(1), 7–10 (2013).
23. T.-H. Liu, S.-P. Yang, Y.-C. Yang, *et al.*, “High-power and low rin performance of a 1.55 μm dfb laser for 10 gb/s satellite optical links,” *IEEE Electron Device Letters* (2023).
24. D. Yang, F. Yan, T. Feng, *et al.*, “Narrow-linewidth and low rin tm/ho co-doped fiber laser based on self-injection locking,” *Opt. Express* **32**(7), 12172–12180 (2024).
25. A. Sano, H. Masuda, T. Kobayashi, *et al.*, “Ultra-high capacity wdm transmission using spectrally-efficient pdm 16-qam modulation and c-and extended l-band wideband optical amplification,” *J. Lightwave Technol.* **29**(4), 578–586 (2011).
26. I. Roberts, J. M. Kahn, and D. Boertjes, “Convex channel power optimization in nonlinear wdm systems using gaussian noise model,” *J. Lightwave Technol.* **34**(13), 3212–3222 (2016).
27. H. Luo, J. Lu, Z. Huang, *et al.*, “Optimization strategy of power control for c+ l+ s band transmission using a simulated annealing algorithm,” *Opt. Express* **30**(1), 664–675 (2022).
28. I. Roberts, J. M. Kahn, J. Harley, *et al.*, “Channel power optimization of wdm systems following gaussian noise nonlinearity model in presence of stimulated raman scattering,” *J. Lightwave Technol.* **35**(23), 5237–5249 (2017).
29. M. A. Amirabadi, M. H. Kahaei, S. A. Nezamalhosseni, *et al.*, “Optimal power allocation in nonlinear mdm-wdm systems using gaussian noise model,” *IET Optoelectron.* **16**(3), 133–148 (2022).
30. M. Secondini, E. Agrell, E. Forestieri, *et al.*, “Nonlinearity mitigation in wdm systems: Models, strategies, and achievable rates,” *J. Lightwave Technol.* **37**(10), 2270–2283 (2019).
31. E. Soltanian, G. Muliuk, S. Uvin, *et al.*, “Micro-transfer-printed narrow-linewidth iii-v-on-si double laser structure with a combined 110 nm tuning range,” *Opt. Express* **30**(22), 39329–39339 (2022).
32. J. Zhang, L. Bogaert, C. Krückel, *et al.*, “Micro-transfer printing inp c-band soas on advanced silicon photonics platform for lossless mzi switch fabrics and high-speed integrated transmitters,” *Opt. Express* **31**(26), 42807–42821 (2023).
33. J. Zhang, L. Bogaert, B. Haq, *et al.*, “Iii-v-on-si dfb laser with co-integrated power amplifier realized using micro-transfer printing,” *IEEE Photonics Technol. Lett.* **35**(11), 593–596 (2023).
34. R. Koscica, Y. Wan, W. He, *et al.*, “Heterogeneous integration of a iii-v quantum dot laser on high thermal conductivity silicon carbide,” *Opt. Lett.* **48**(10), 2539–2542 (2023).
35. J. Justice, C. Bower, M. Meitl, *et al.*, “Wafer-scale integration of group iii-v lasers on silicon using transfer printing of epitaxial layers,” *Nat. Photonics* **6**(9), 610–614 (2012).
36. J. M. Ramírez, P. Fanneau de la Horie, J.-G. Provost, *et al.*, “Low-threshold, high-power on-chip tunable iii-v/si lasers with integrated semiconductor optical amplifiers,” *Appl. Sci.* **11**(23), 11096 (2021).
37. R. Kazarinov and C. Henry, “The relation of line narrowing and chirp reduction resulting from the coupling of a semiconductor laser to passive resonator,” *IEEE J. Quantum Electron.* **23**(9), 1401–1409 (1987).
38. S. Dey and S. Mandal, “Modeling and analysis of quadruple optical ring resonator performance as optical filter using vernier principle,” *Opt. Commun.* **285**(4), 439–446 (2012).
39. M. A. Tran, D. Huang, and J. E. Bowers, “Tutorial on narrow linewidth tunable semiconductor lasers using si/iii-v heterogeneous integration,” *APL Photonics* **4**(11), 111101 (2019).
40. J. Guo, C. A. McLemore, C. Xiang, *et al.*, “Chip-based laser with 1-hertz integrated linewidth,” *Sci. Adv.* **8**(43), eabp9006 (2022).
41. B. Pan, J. Bourderionnet, V. Billault, *et al.*, “Iii-v-on-si₃n₄ widely tunable narrow-linewidth laser based on micro-transfer printing,” *Photonics Res.* **12**(11), 2508–2520 (2024).
42. J. Wang, X. Li, X. Guo, *et al.*, “Scalable single-microring hybrid iii-v/si lasers for emerging narrow-linewidth applications,” *Opt. Express* **32**(15), 26751–26762 (2024).
43. T. Simpson, J. Liu, and A. Gavrielides, “Small-signal analysis of modulation characteristics in a semiconductor laser subject to strong optical injection,” *IEEE J. Quantum Electron.* **32**(8), 1456–1468 (1996).
44. G. Morthier, R. Schatz, and O. Kjebon, “Extended modulation bandwidth of dbr and external cavity lasers by utilizing a cavity resonance for equalization,” *IEEE J. Quantum Electron.* **36**(12), 1468–1475 (2000).
45. G. Morthier, G. Sarlet, R. Baets, *et al.*, “The direct modulation bandwidth of widely tunable dbr laser diodes,” in *Conference Digest. 2000 IEEE 17th International Semiconductor Laser Conference. (Cat. No. 00CH37092)*, (IEEE, 2000), pp. 87–88.